

The Mass-Concentration-Redshift Relation of Cold Dark Matter Halos

Aaron D. Ludlow^{1,*}, Julio F. Navarro², Raúl E. Angulo³, Michael Boylan-Kolchin⁴, Volker Springel^{5,6}, Carlos Frenk⁷, Simon D. M. White⁸

¹Argelander-Institut für Astronomie, Auf dem Hügel 71, D-53121 Bonn, Germany

²Senior CIFAR Fellow, Dept. of Physics and Astronomy, University of Victoria, Victoria, BC, V8P 5C2, Canada

³Centro de Estudios de Física del Cosmos de Aragón, Plaza San Juan 1, Planta-2, 44001, Teruel, Spain

⁴Department of Astronomy and Joint Space-Science Institute, University of Maryland, College Park, MD, 20742-2421, USA

⁵Heidelberg Institute for Theoretical Studies, Schloss-Wolfsbrunnengasse 35, 69118 Heidelberg, Germany

⁶Zentrum für Astronomie der Universität Heidelberg, ARI, Mönchhofstr. 12-14, 69120 Heidelberg, Germany

⁷Institute for Computational Cosmology, Dept. of Physics, Univ. of Durham, South Road, Durham DH1 3LE, UK

⁸Max-Planck-Institut für Astrophysik, Karl-Schwarzschild-Straße 1, 85740 Garching bei München, Germany

5 December 2013

ABSTRACT

We use the Millennium Simulation series to investigate the mass and redshift dependence of the concentration of equilibrium cold dark matter (CDM) halos. We extend earlier work on the relation between halo mass profiles and assembly histories to show how the latter may be used to predict concentrations for halos of all masses and at any redshift. Our results clarify the link between concentration and the “collapse redshift” of a halo as well as why concentration depends on mass and redshift solely through the dimensionless “peak height” mass parameter, $\nu(M, z) = \delta_{\text{crit}}(z)/\sigma(M, z)$. We combine these results with analytic mass accretion histories to extrapolate the $c(M, z)$ relations to mass regimes difficult to reach through direct simulation. Our model predicts that, at given z , $c(M)$ should deviate systematically from a simple power law at high masses, where concentrations approach a constant value, and at low masses, where concentrations are substantially lower than expected from extrapolating published empirical fits. This correction may reduce the expected self-annihilation boost factor from substructure by about one order of magnitude. The model also reproduces the $c(M, z)$ dependence on cosmological parameters reported in earlier work, and thus provides a simple and robust account of the relation between cosmology and the mass-concentration-redshift relation of CDM halos.

Key words: cosmology: dark matter – methods: numerical

1 INTRODUCTION

It is now well established that the equilibrium density profile of cold dark matter (CDM) halos is nearly self-similar, and may be well approximated by scaling a simple formula (Navarro et al. 1996, 1997, hereafter NFW):

$$\frac{\rho(r)}{\rho_{\text{crit}}} = \frac{\delta_c}{(r/r_s)(1+r/r_s)^2}. \quad (1)$$

This profile is referred to in the literature as the “NFW profile” and is characterized by a scale radius, r_s , and an overdensity, δ_c . These scaling parameters may also be expressed

in terms of the halo virial¹ mass, M_{200} , and a dimensionless “concentration” parameter, $c = r_{200}/r_s$, defined as the ratio between the virial and scale radius of a halo. The scale radius indicates where the logarithmic slope of the profile has the isothermal value of -2 , and therefore, we shall hereafter use indistinctly r_{-2} or r_s to denote this radius. The concentration is an alternative measure of the halo characteristic density, and at a given halos mass the two are related by

¹ We define the virial parameters of a halo as those measured within a sphere centered at the potential minimum that encloses a mean density $200\times$ the critical density for closure, $\rho_{\text{crit}}(z) = 3H(z)^2/8\pi G$, and label them with a “200” subscript. For example, r_{200} and M_{200} are the halo’s virial radius and mass, respectively.

* E-mail: aludlow@astro.uni-bonn.de

$$\delta_c = \frac{200}{3} \frac{c^3}{[\ln(1+c) - c/(1+c)]}. \quad (2)$$

As noted in the original NFW papers, mass and concentration are strongly correlated, albeit with considerable scatter.

Since, together, mass and concentration fully specify the equilibrium mass profile of a halo, there has been considerable interest in understanding the origin of such correlation, as well as its dependence on redshift and on cosmological parameters. At given redshift, concentration decreases monotonically with increasing halo mass in a manner that suggests a link between the characteristic density of a halo and the time of its assembly. Indeed, NFW showed that the main trends in the mass-concentration relation, $c(M)$, could be reproduced by a simple model where the characteristic density of a halo reflects the critical density of the universe at a suitably defined “collapse redshift”. The NFW model identified a halo’s collapse redshift with the time at which half the mass of the halo was first contained in progenitors more massive than some fraction, f , of its final mass. This model, however, yields acceptable results only for surprisingly small values of f , of order one percent.

The NFW prescription also predicts that, at given mass, concentrations should evolve weakly with redshift, at odds with the stronger dependence on redshift reported in later work. Bullock et al. (2001), for example, argued that concentrations of halos of fixed mass should scale linearly with expansion factor; $c \propto a$. Eke et al. (2001), on the other hand, proposed that concentrations should depend both on the amplitude as well as on the shape of the power spectrum. Their predictions, however, also failed to reproduce the findings of subsequent simulation work. It has now become clear that concentration depends on mass and redshift in a complex fashion; for example, although the concentration of rare, very massive halos barely evolves with redshift, that of low mass halos evolves rapidly (see, e.g., Gao et al. 2008).

The latter behavior is better reproduced by models that link the concentration of a halo with its past accretion history (Wechsler et al. 2002; Zhao et al. 2003; Lu et al. 2006). In these models the concentration is empirically found to trace the time when halos transition from a period of “fast growth” to another where mass is accreted more gradually. These empirical models are able to account for the nearly constant² concentration of very massive halos (they are all still in the fast-growth phase) and for the redshift dependence of the concentration at different halo masses.

Attempts to formalize these results into an analytic model have been less successful. For example, as in the original NFW papers, the model of Zhao et al. (2009) links the concentration with a time when a halo had only assembled a surprisingly small ($\sim 4\%$) fraction of its final mass. This casts into doubt how the model should be interpreted, or how it should be extended to halo mass regimes or cosmological parameters not calibrated directly by simulation.

² Recently, Prada et al. (2012) have argued for an “upturn” in the concentration of very massive halos. This has now been shown to be due to unrelaxed halos in transient stages of their evolution (Ludlow et al. 2012). The upturn disappears when only relaxed halos are considered.

Table 1. Numerical properties of the Millennium and Aquarius simulations. N_p is the total number of particles; L_{box} is the simulation boxsize; ϵ is the Plummer-equivalent gravitational force softening and m_p is the particles mass. In the case of the Aquarius runs N_p is the number of high-resolution particles and m_p is their mass.

Simulation	N_p	L_{box} [Mpc/h]	ϵ [kpc/h]	m_p [M_\odot/h]
MS-XXL	6720^3	3000	10	6.17×10^9
MS-I	2160^3	500	5	8.61×10^8
MS-II	2160^3	100	1	6.89×10^6
Aq-A-2	5.3×10^8	-	0.050	1.00×10^4
Aq-A-1	4.3×10^9	-	0.015	1.25×10^3

We have recently used the Millennium Simulation series of cosmological simulations to revisit these issues (Ludlow et al. 2013). The key result of that work is that the *shape* of the mass accretion history of a halo (hereafter MAH for short) is indistinguishable from the *shape* of its mass profile at the final time. The similarity in shape becomes readily apparent when expressing the evolution of the mass of the main progenitor in terms of the critical density rather than redshift, $M(\rho_{\text{crit}}(z))$, and the mass profile in terms of enclosed mass and mean inner density, $M(\langle \rho(< r) \rangle)$. Both shapes resemble closely the NFW profile.

This insight provides a compelling explanation for the NFW profile and its self-similar nature, which can be traced to the mass invariance of halo mass accretion histories (see, e.g., van den Bosch 2002). For given halo mass, its average mass accretion history may be fully described by specifying a single “concentration” parameter, c_{MAH} , and there is a unique correspondence between this parameter and the NFW concentration parameter, c_{NFW} , of the halo mass profile. Once this relation has been calibrated, concentrations may be predicted for halos of any mass and at any redshift, and for any cosmology, provided that accurate mass accretion histories are available.

We explore these issues here by extending our earlier $z = 0$ analysis of the Millennium Simulation series to higher redshift. We use this analysis to calibrate the $c_{\text{MAH}}-c_{\text{NFW}}$ relation and to show how analytic mass accretion histories may be used to predict concentration-mass relations that are in full agreement with published results.

We begin with a brief summary of the Millennium Simulation series (Sec. 2) and of our analysis technique (Sec. 3), followed by a presentation of our main results in Sec. 4. We conclude with a brief summary of our main conclusions in Sec. 5.

2 NUMERICAL SIMULATIONS

Our analysis uses spherically-averaged mass profiles and mass accretion histories of dark matter halos identified in the Millennium Simulation suite: MS-I (Springel et al. 2005), MS-II (Boylan-Kolchin et al. 2009), and MS-XXL (Angulo et al. 2012) (hereafter referred to collectively as

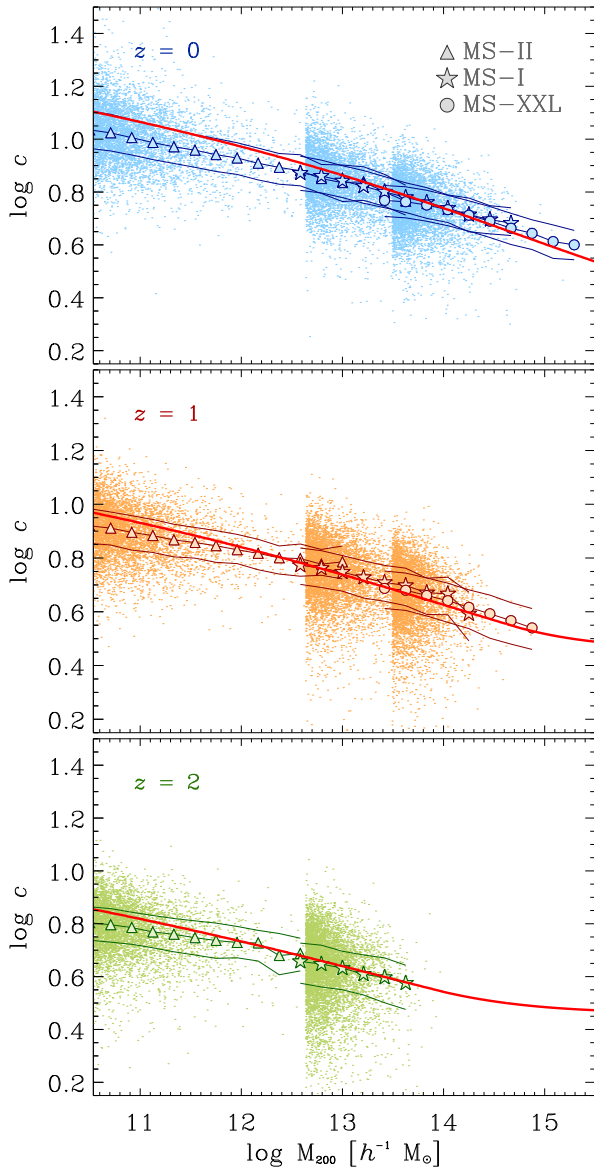


Figure 1. Mass and redshift dependence of best-fit NFW concentrations for all relaxed MS halos with more than 5000 particles within the virial radius. From top to bottom, panels correspond to halos identified at $z_i = 0, 1$ and 2 , respectively. Individual halos are shown as colored dots; heavy filled symbols show the median trends for each simulation (see legend); 25th and 75th percentiles are shown as thin lines. The solid red line in each panel shows the mass-concentration relation obtained from fitting NFW profiles to the mass accretion histories predicted by the model described in the Appendix. See Secs. 4.3 and 4.4 for more details.

MS). Here we provide a brief description of the simulations and their associated halo catalogs, and refer the interested reader to those papers for further details.

2.1 The Millennium Runs

The three MS runs adopt the same snapshot output sequence and cosmological parameters, which were chosen to

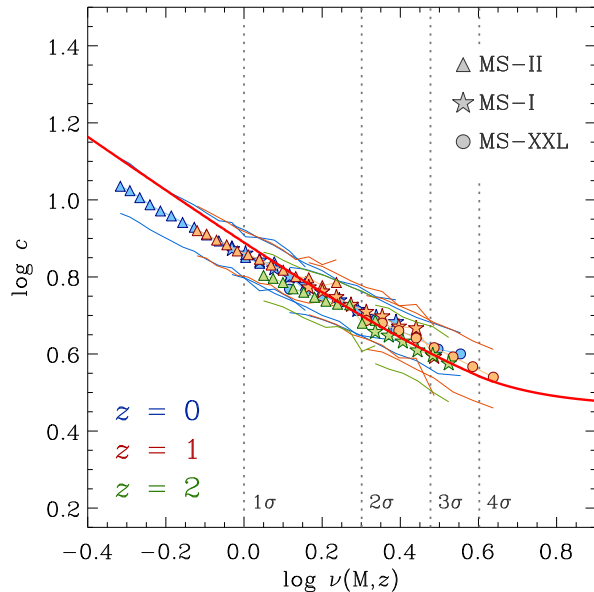


Figure 2. Halo concentrations shown as a function of the dimensionless mass parameter, $\nu = \delta_{\text{crit}}(z)/\sigma(M, z)$ for all three redshifts shown in Fig. 1. Heavy symbols show the same median trends as in Fig. 1 for each simulation, as indicated in the legend; thin lines show the 25th and 75th percentiles. The solid red line shows the $c(\nu)$ relation predicted using the model described in the Appendix (see Secs. 4.3 and 4.4 for details).

Table 2. Summary of the parameters adopted for the cosmological models mentioned in this paper. All models assume a flat geometry, so that $\Omega_\Lambda = 1 - \Omega_M$.

Cosmology	Ω_M	Ω_{bar}	σ_8	h	n_s
Millennium	0.250	0.045	0.90	0.73	1.0
WMAP 1	0.268	0.044	0.90	0.71	1.0
WMAP 3	0.238	0.042	0.75	0.73	0.95
WMAP 5	0.258	0.0441	0.796	0.719	0.963
WMAP 7	0.270	0.0469	0.82	0.70	0.95
Planck	0.3086	0.0483	0.8288	0.6777	0.9611

be consistent with a WMAP-1 LCDM model: $\Omega_M = 0.25$; $\Omega_\Lambda = 1 - \Omega_M = 0.75$; $\sigma_8 = 0.9$; $n_s = 1$; $h = 0.73$. Here Ω_i is the contribution to the current matter-energy density of the Universe from component i , expressed in units of the critical density for closure; σ_8 is the rms mass fluctuation in $8 h^{-1}$ Mpc spheres, linearly extrapolated to $z = 0$; n_s is the spectral index of primordial density fluctuations; and h is the present-day Hubble expansion rate in units of $100 \text{ km s}^{-1} \text{ Mpc}^{-1}$.

The MS-I and MS-II evolved the dark matter density field using $N_p = 2160^3$ particles; these runs differ only in box size, L_{box} , Plummer-equivalent force softening, ϵ , and particle mass, m_p . MS-XXL is the largest of the three runs both in particle number, $N_p = 6720^3$, and in box size, $L_{\text{box}} = 3 h^{-1} \text{ Gpc}$. Because of its size, however, MS-XXL particle data was not stored for all snapshot redshifts. We list the most important numerical parameters of these simulations in Table 1.

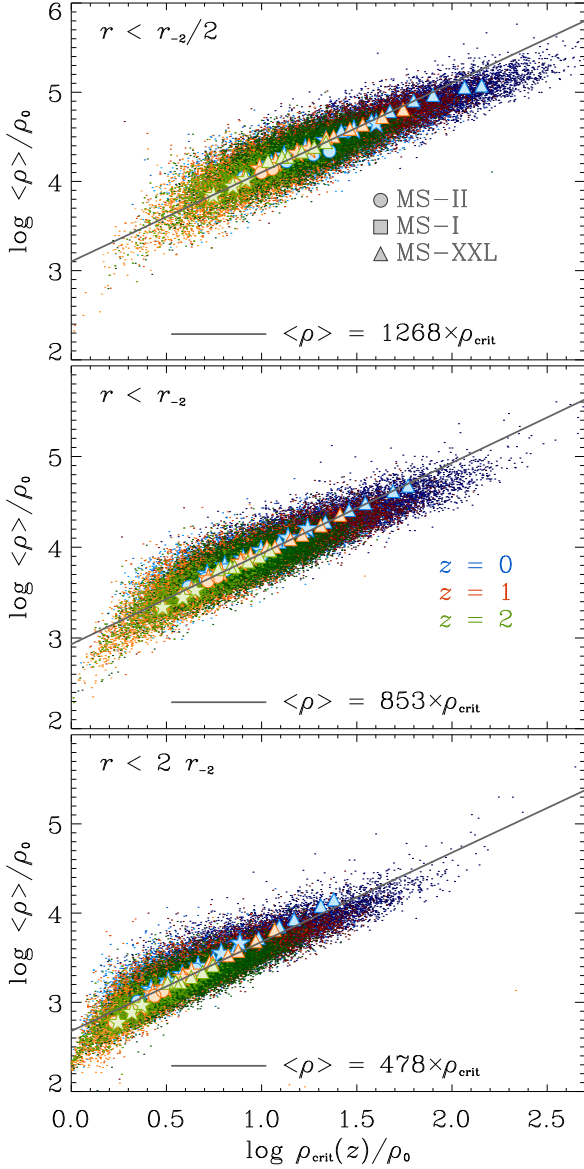


Figure 3. The mean enclosed density, $\langle \rho_{-2} \rangle$, within the NFW scale radius, r_{-2} (middle panel), as well as within $r_{-2}/2$ (top panel) and $2 \times r_{-2}$ (bottom panel), shown as a function of the critical density of the Universe at the time when the main progenitor first reaches the mass enclosed within each of those radii. Critical densities are scaled to the value at which a halo is identified, $\rho_0 \equiv \rho_{\text{crit}}(z_i)$. Only relaxed halos with more than 20000 particles identified at redshifts $z_i = 0$ (blue points), 1 (red points) and 2 (green points) are shown in order to minimize overlap. Note the direct proportionality between the two densities that holds in all panels. This implies that mass accretion histories can be reconstructed from the mass profiles and vice versa. Individual halos are shown as colored dots; large filled symbols show the results obtained after averaging halo mass profiles and accretion histories in logarithmic mass bins of width $\delta \log M = 0.4$.

2.2 Dark Matter Halo Catalogs

Dark matter halos were identified in each simulation output using a friends-of-friends (FOF) halo finder with a link-length $b = 0.2$ times the mean inter-particle separation. The subhalo finder SUBFIND (Springel et al. 2001) was then run on each FOF group that contained at least $N_{\text{min}} = 20$ particles in order to identify its self-bound substructures. SUBFIND outputs a number of useful characteristics for each FOF group and its subgroups. We retain for our analysis only the main halo of each FOF group (i.e., we do not consider substructure halos) and record their virial mass, M_{200} , as well as the radius, r_{max} , of the peak circular velocity, V_{max} . We note that M_{200} refers to the *total* mass within r_{200} , including substructure. For a halo that follows the NFW profile, V_{max} and r_{max} are fully determined by the virial mass and concentration, and therefore may also be used as alternative parameters to express the halo mass profile.

Because of the dynamical nature of the formation process, DM halos are, at best, quasi-equilibrium systems. We therefore compute three diagnostics that can be used to flag halos that are far from equilibrium. Including halos in such transient states in the analysis can lead to biased estimates of their mean structural properties, especially at large halo masses, where a majority of the systems may be out of equilibrium (e.g., Neto et al. 2007; Macciò et al. 2008; Ludlow et al. 2012). The “relaxation” diagnostics are: (i) the substructure mass fraction, $f_{\text{sub}} = M_{\text{sub}}(< r_{200})/M_{200}$, (ii) the center of mass offset from the potential minimum, $d_{\text{off}} = |\mathbf{r}_p - \mathbf{r}_{\text{CM}}|/r_{200}$, and (iii) the virial ratio of kinetic to potential energies, $2K/|U|$. In the analysis that follows we shall only consider halos that simultaneously satisfy the following three conditions: i) $f_{\text{sub}} < 0.1$, ii) $d_{\text{off}} < 0.07$, and iii) $2K/|U| < 1.35$.

The relative importance of unrelaxed halos increases with halo mass and with redshift, reflecting the more recent assembly of rarer, more massive structures. For example, fewer than 50% of halos with virial mass in excess of $\sim 10^{14} h^{-1} M_{\odot}$ pass our three relaxation criteria at $z = 0$. By $z = 1$, this fraction decreases to $\sim 20\%$. Similarly, roughly 80% of halos with present-day virial mass of order $10^{12} h^{-1} M_{\odot}$, meet our three relaxation criteria. For the same mass scale, the fraction decreases to $\sim 52\%$ at $z = 1$; by $z = 2$ only about one third of these systems are deemed relaxed. We exclude unrelaxed halos from our analysis since they are only poorly approximated by simple fitting formulae like the NFW profile, and because their transient state means that their fit parameters change quickly, hampering interpretation.

3 ANALYSIS

3.1 Mass Profiles and Accretion Histories

We have computed spherically-averaged density profiles and mass accretion histories for relaxed halos identified at three different redshifts: $z_i = 0, 1$, and 2. Density profiles are computed in 32 radial bins that span the range $-2.5 < \log r/r_{200} < 0$ in equally spaced steps in $\log r$. Within each radial bin we also compute the total enclosed mass, $M(r)$ (including substructure), and the mean inner density, $\langle \rho \rangle(r) = M(r)/(4/3)\pi r^3$. In order to obtain robust esti-

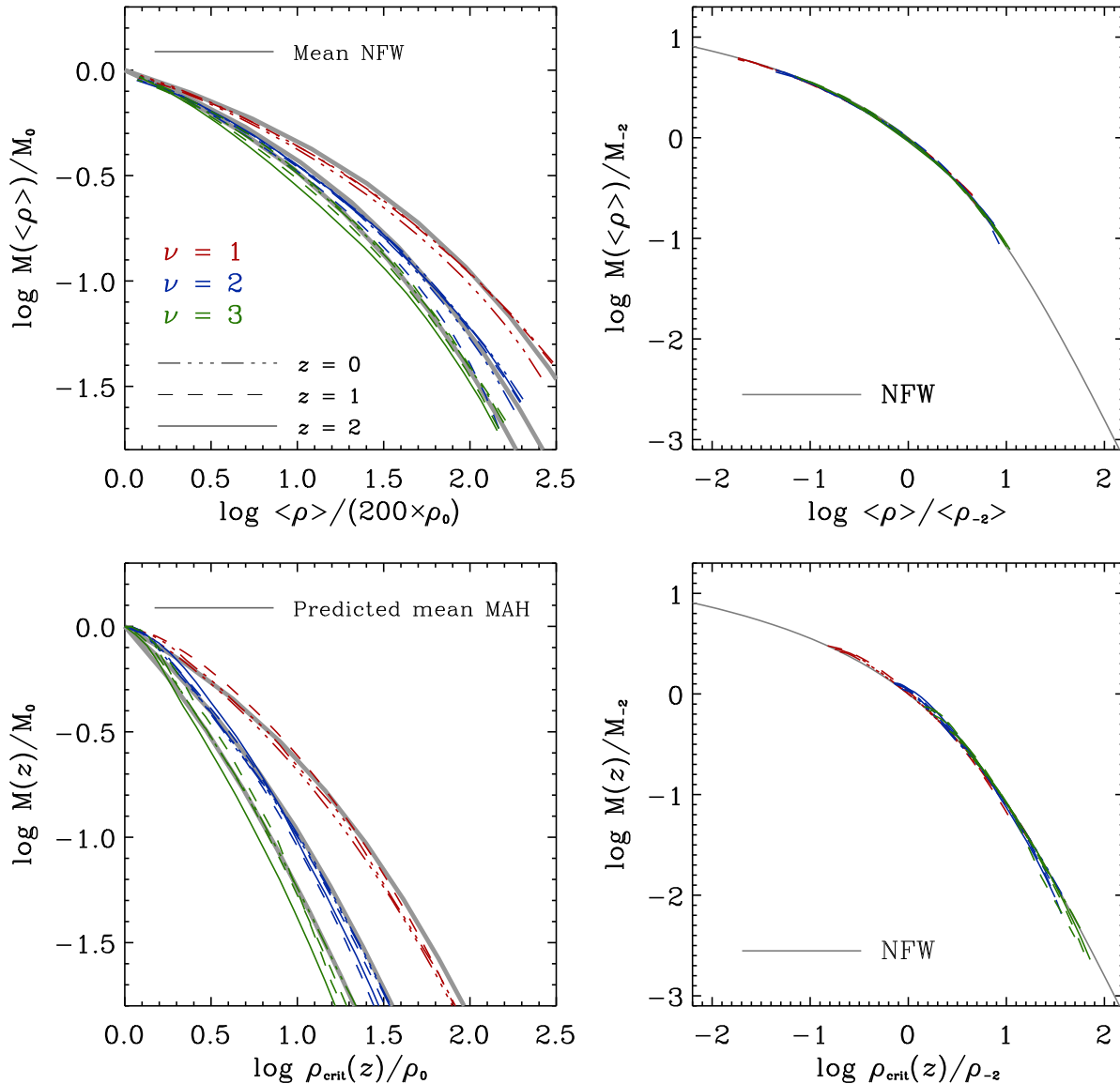


Figure 4. Average mass profiles and accretion histories for halos with dimensionless mass parameter values equal to $\nu = 1$ (red), 2 (blue), and 3 (green). Different line styles correspond to halos identified at different redshifts. Top panels show enclosed mass versus mean inner density profiles; bottom panels show the growth of the mass of the main progenitors as a function of redshift, expressed in units of the critical density. All masses are scaled to the final mass of the halo at the time of identification. Densities in the bottom left panel are scaled to the critical density at the identification redshift, $\rho_0 = \rho_{\text{crit}}(z_i)$. Densities in the top left panel are scaled to the mean enclosed density at the virial radius, $200 \times \rho_0$. The top right-hand side panel shows the same profiles as on the left, but scaled to the mass and density within the scale radius of the best-fitting NFW profile. The bottom right shows the same curves as on the left, scaled, as in the top-right panel, to the characteristic mass and density of the NFW best fit. Note that, independent of halo mass and of identification redshift, both the mass profiles and accretion histories follow closely the same NFW shape. Note as well that the accretion histories of all halos with the same value of ν are similar, regardless of redshift.

mates of the structural parameters of the halo mass profiles, we restrict our analysis to systems that contain at least 5000 particles within their virial radius, r_{200} . Even with these strict limits there are many thousands of halos in our sample at each redshift: at $z_i = 0$ about 1.1 million halos are included in our sample. At $z_i = 1$ and 2, the numbers go down to roughly 300000 and 32000, respectively. (MS-XXL

is excluded from our $z_i = 2$ analysis because particle data is unavailable for this redshift.)

We compute the mass accretion history (MAH) of each halo identified at z_i by tracking the virial mass of its main progenitor through all previous simulation outputs. Although other operational definitions of assembly histories exist (see, e.g. Wang et al. 2011; Giocoli et al. 2012), ours is simple to compute both in simulations as well as in

semi-analytic models for structure formation, such as those based on excursion-set theory (Kauffmann & White 1993; Lacey & Cole 1993; Eisenstein & Loeb 1996; Nusser & Sheth 1999; Somerville & Kolatt 1999).

As mentioned in Sec. 1, although the MAH is most often written as a function of redshift or expansion factor, we will instead express it in terms of the critical density of the Universe; i.e., as $M(\rho_{\text{crit}}(z))$. This facilitates a comparison between the *shape* of the mass accretion history and that of mass profile, which we write in terms of the mean enclosed density, $M(\langle\rho\rangle)$.

3.2 NFW Profiles and Fitting Techniques

We estimate halo structural parameters by fitting eq. (1) to the mass profiles of the full sample of equilibrium halos described above. The NFW profile has two free parameters, which are simultaneously adjusted in order to minimize the figure-of-merit function

$$\psi^2 = \frac{1}{N_{\text{bin}}} \sum_{i=1}^{N_{\text{bin}}} [\ln \rho_i - \ln \rho_{\text{NFW}}(\delta_c; r_s)]^2. \quad (3)$$

In order to avoid biases that may be introduced by substructures in the outskirts of the halo we restrict our fits to the radial range $r_{\text{min}} < r < 0.6 r_{200}$, where r_{min} is chosen to be either the “convergence” radius, r_{conv}^3 , or $0.05 \times r_{200}$, whichever is smaller (for a more detailed discussion of the implications of limiting the outer fit radius please see Ludlow et al. 2010). In general, NFW fits to the spherically averaged $\rho(r)$ profiles are good: at $z = 0$, for example, ψ_{min} has a median value of $0.083_{-0.016}^{+0.019}$, where the quoted range indicates the upper and lower quartiles of the distribution. Similarly good fits are obtained at redshifts $z_i = 1$ and 2. The best-fit NFW profiles yield estimates of the halo structural parameters δ_c and r_s for each halo in our sample, which we use in turn to estimate c_{NFW} , the concentration parameter.

As discussed above, NFW profiles can also be fit to halo mass accretion histories in order to estimate their “concentration” parameter (Ludlow et al. 2013). We do so by fitting the MAH, written as $M(\rho_{\text{crit}})$, with the NFW profile expressed in terms of the enclosed density:

$$\langle\rho\rangle(r) = \frac{3M(<r)}{4\pi r^3} = \frac{200}{x^3} \frac{g(cx)}{g(c)} \rho_{\text{crit}}, \quad (4)$$

where $x \equiv r/r_{200}$ and $g(y) = \ln(1+y) - y/(1+y)$. Since we are interested in estimating a single parameter, the concentration, we first normalize the MAH to the halo virial mass, $M_0 = M(z_i)$, and critical density, $\rho_0 = \rho_{\text{crit}}(z_i)$, at the redshift of interest, and then determine the value of the remaining parameter, c_{MAH} , by minimizing the rms deviation between eq. (4) and the MAH.

³ The “convergence radius” is defined here as in Power et al. (2003).

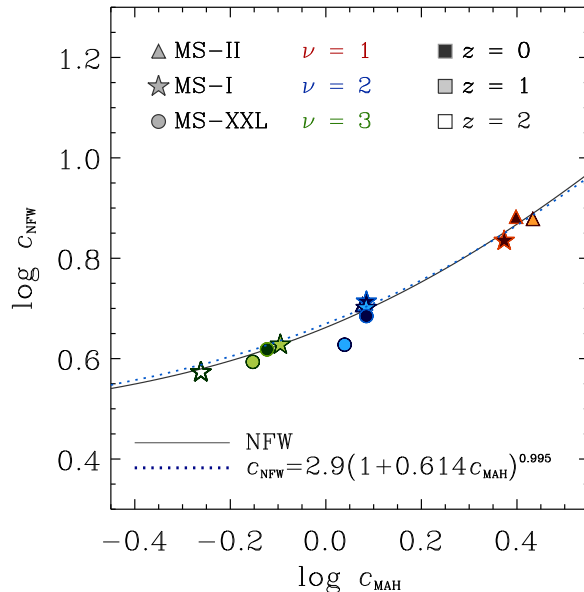


Figure 5. Relation between the concentration parameters obtained from NFW fits to the mass profiles (c_{NFW}) and accretion histories (c_{MAH}) shown in Figure 4. Individual points are colored according to peak height, ν ; filled or open symbols indicate the redshift and simulation of each halo sample, as indicated in the legend. The solid curve shows the relation expected given the correlations shown in the middle panel of Fig. 3; the dotted line shows a useful approximation to this curve: $c_{\text{NFW}} = 2.9 \times (1 + 0.614 c_{\text{MAH}})^{0.995}$.

4 RESULTS

4.1 The mass-concentration-redshift relation

The mass-concentration relation, $c(M)$, is shown in Fig. 1 for equilibrium halos identified at $z_i = 0, 1$, and 2. The heavy symbols trace the median trend for each halo sample, and the thin lines delineate the 25th and 75th percentile range. Note the excellent agreement between different simulations in the mass intervals where they overlap, a clear demonstration that our results are not compromised by numerical artifact. We find, in agreement with earlier work, that the concentration is a monotonic⁴ but weak function of mass, varying by only a factor of ~ 4 over the 6 decades in mass resolved by the simulations at $z = 0$. Concentrations decrease systematically with increasing redshift over the mass range resolved here, although the magnitude of the decrease is mass-dependent: from $z = 0$ to $z = 2$ concentrations decrease by about a factor of 1.6 for $10^{11} h^{-1} M_{\odot}$ halos but less than 50% for $10^{14} h^{-1} M_{\odot}$ halos.

This seemingly complex mass-dependent evolution actually reflects a simpler dependence, which becomes apparent when expressing concentrations in terms of the dimensionless “peak height” mass parameter,

$$\nu(M, z) = \delta_{\text{crit}}(z)/\sigma(M, z), \quad (5)$$

⁴ The “plateau” in concentration at large halo masses reported in earlier work is not apparent here because we are only considering relaxed halos; including unrelaxed massive halos raises the median concentration. See Ludlow et al. (2012) for further details.

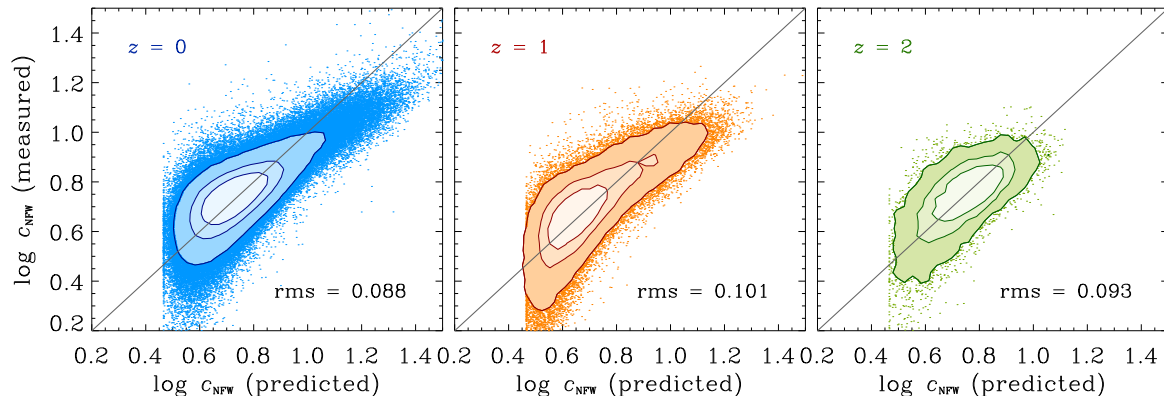


Figure 6. A halo-to-halo comparison of the measured concentrations and those predicted by fitting NFW profiles to the mass accretion histories and using the relation shown in Fig. 5. Contours enclose 50, 75 and 95 percent of the halos, with the remaining 5 percent shown as individual points. The rms scatter in the ratio of measured-to-predicted concentration is given in each panel.

defined as the ratio between the critical overdensity for collapse at redshift z and the linear rms fluctuation at z in spheres of mass M . The larger ν the rarer the halo, and the more massive it is in relation to the characteristic clustering mass, M_* , defined by $\nu(M_*) = 1$.

Fig. 2 shows that concentrations depend primarily on ν , over the entire range of masses and redshifts analyzed here (for a similar result, see also Prada et al. 2012, and references therein). This result is consistent with the rescaling procedure outlined by Angulo & White (2010) to match the outcome of simulations adopting slightly different power spectra and cosmological parameters. It also offers an important clue that any successful analytical model of the mass-concentration-redshift relation should reproduce⁵. The thick red lines in Figs. 1 and 2 present the predictions of one such model, which we discuss in detail in Sec. 4.4 below.

4.2 MAH and Mass Profiles

As discussed by Ludlow et al. (2013), the shape of the mass profiles of MS halos identified at $z = 0$ is intimately related to their accretion histories. We show in Fig. 3 that this result also applies to halos identified at higher redshift. The middle panel of this figure plots the mean density enclosed within the NFW scale radius, $\langle \rho_{-2} \rangle = M_{-2}/(4/3)\pi r_{-2}^3$, versus $\rho_{\text{crit}}(z_{-2})$, the critical density of the Universe at the time when the mass of the main progenitor halo equals M_{-2} . Results for all three identification redshifts are included, after scaling densities to the critical density at each z_i , $\rho_0 \equiv \rho_{\text{crit}}(z_i)$.

Note that the two densities scale linearly, and that there is no difference between halos selected at different z_i . A similar result is found when repeating the exercise within a radius equal to one half or twice the scale radius (top and bottom panels of Fig. 3, respectively). This confirms that

mass accretion histories can be reconstructed from the mass profile, and vice versa, for halos selected at any redshift.

Further, as Fig. 4 makes clear, mass accretion histories and mass profiles have the *same* shape on average, which can be closely approximated by the NFW profile. In this figure, the similarity becomes apparent when comparing MAHs expressed as $M(\rho_{\text{crit}})$ with mass profiles expressed as $M(\langle \rho \rangle)$. Each of these profiles, shown for different values of ν in the left panels, can be scaled to the characteristic values of their best NFW fits. This is shown in the right-hand panels, which puts in evidence the remarkable similarity between MAH and mass profile shapes.

Fig. 4 also shows that average accretion histories are solely a function of the dimensionless mass parameter ν . Indeed, regardless of the identification redshift, the scaled mass accretion histories of halos with the same value of ν are essentially indistinguishable from each other. This explains why concentrations depend only on ν , as shown in Fig. 2: accretion histories fully determine the final mass profile of a halo and, since MAHs depend only on ν , so do concentrations.

The results discussed above imply that one may use halo mass profiles to predict, on average, their MAH. Since both are well approximated by the NFW profile, all that is needed, for given halo mass, is to calibrate the relation between the MAH “concentration” and that of the mass profile. This may be derived analytically from the proportionality constant between $\langle \rho_{-2} \rangle$ and $\rho_{\text{crit}}(z_{-2})$ shown in the middle panel of Fig. 3. The result is shown by the solid line in Fig. 5, together with a simple approximation,

$$c_{\text{NFW}} = 2.9 (1 + 0.614 c_{\text{MAH}})^{0.995}, \quad (6)$$

that proves accurate over the range of concentrations probed by our simulations.

A couple of points are worth remarking about this relation. The first is that it predicts a minimum concentration ($c_{\text{NFW}} \sim 2.9$) for halos that form relatively recently and whose MAH, consequently, is best described with a very low value of c_{MAH} . This is broadly consistent with the idea, first proposed by NFW, that there should be little difference in the concentration of very massive systems ($M \gg M_*$), if concentration in any way reflects the formation time. In-

⁵ Note that halo collapse times (and therefore concentrations) may also depend on the expansion history of the Universe (Dolag et al. 2004). A residual, but weak, dependence on the shape of the linear growth factor might therefore become evident for expansion histories that differ significantly from Λ CDM.

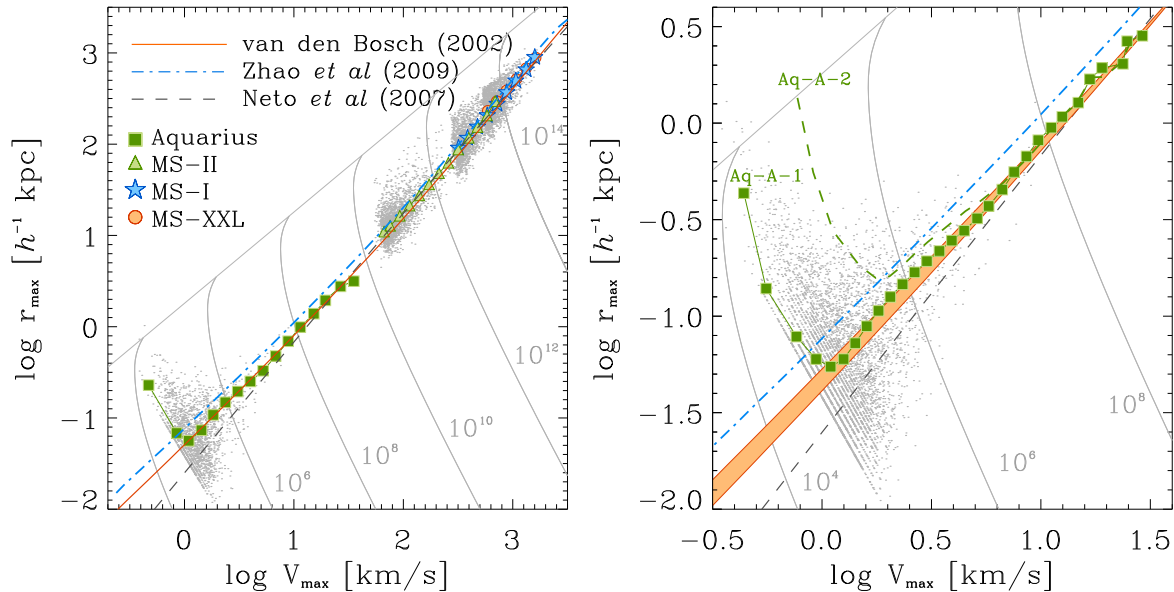


Figure 8. *Left panel:* Relation between r_{\max} and V_{\max} at $z = 0$ for isolated dark matter halos in the Millennium Simulations and in the Aq-A *simulation* of the Aquarius Project (Springel et al. 2008). Individual halos are shown by the grey points; grey curves indicate halos of constant virial mass, labeled in units of $h^{-1} M_{\odot}$. Heavy symbols trace the median r_{\max} and V_{\max} , computed in equally spaced logarithmic bins of halo mass. The upturn in the Aquarius relation at low masses indicates the onset of artifacts induced by limited numerical resolution. The gray dashed line indicates the r_{\max} - V_{\max} relation corresponding to the power-law $c(M)$ relation derived by Neto et al. (2007) from halos in the MS-I simulation. The solid orange line shows the relation predicted by NFW-fitting the mass accretion histories of van den Bosch (2002); the dot-dashed blue line corresponds to MAHs predicted by Zhao et al. (2009). *Right panel:* A zoom-in of the left panel showing only isolated halos in the Aquarius simulation. These are defined as systems that, at $z = 0$, lie at least three virial radii away from the main Aquarius halo. Symbols and lines are as in the left. The orange shaded area shows how the van den Bosch (2002) relation changes when varying the MAH range fitted; from $10^{-3} < M/M_0 < 0.8$ (top) to $0.1 < M/M_0 < 0.8$ (bottom).

deed, since all of these halos must be collapsing just before the time at which they are identified, they share a common assembly time and should therefore have similar concentrations⁶.

The second point to note about eq. (6) is that the c_{NFW} dependence on c_{MAH} is quite shallow, implying that even large changes in MAH lead to modest changes in mass profiles. We show one application of this relation in the bottom-left panel of Fig 4. The thick grey lines in this panel show the *predicted* MAHs corresponding to the mass profiles shown in the upper-left panel, using eq. (6). The predictions match the actual MAHs measured in the simulations quite well.

The procedure can also be reversed, so that accretion histories may be used to predict mass profile concentrations. We show this in Fig. 6, where we compare, for each identification redshift, the concentrations measured in the simulations with estimates obtained by fitting *individual* halo accretion histories and then using eq. (6) to predict c_{NFW} . As Fig. 6 makes clear, the predicted concentrations for re-

laxed halos are in good agreement with measured ones; the rms between predicted and measured values is only of order $\sim 25\%$. This is remarkable, given the fact that (i) individual MAH are often complex and at times not even monotonic, with several local maxima caused by distinct merger events, and (ii) that our model attempts to describe them with a *single* parameter.

4.3 Model Mass Accretion Histories

The results of the previous subsection imply that the concentration-mass-redshift relation can be predicted analytically provided that accurate mass accretion histories are available. In the recent past, this topic has received considerable attention, which has led to the development of sophisticated algorithms able to compute accretion histories that agree very well with the results of cosmological N-body simulations, for arbitrary halo masses, redshift, power spectra, and cosmological parameters. Analytic models based on extensions of the Press & Schechter (1974) formalism, for example, have been used extensively to predict halo formation times, progenitor mass distributions, halo merger rates, and other statistics (Bond et al. 1991; Bower 1991; Lacey & Cole 1993; Kauffmann & White 1993; Somerville & Kolatt 1999; Sheth & Lemson 1999; Parkinson et al. 2008). Other methods follow the hierarchical build-up of dark matter halos using Lagrangian perturbation theory (e.g. Taffoni et al. 2002;

⁶ Very massive ($\nu \gtrsim 3$) halos actually deviate slightly but systematically from the above trends; see, for example, how halos with the smallest values of $\langle \rho_{-2} \rangle$ fall below the fitted relation in Fig. 3. Indeed, their MAH shapes differ slightly, but systematically, from NFW (Ludlow et al. 2013). As discussed by Gao et al. (2008), the mass profiles of these systems also deviate from NFW and are better described by Einasto profiles with large values of the Einasto parameter α .

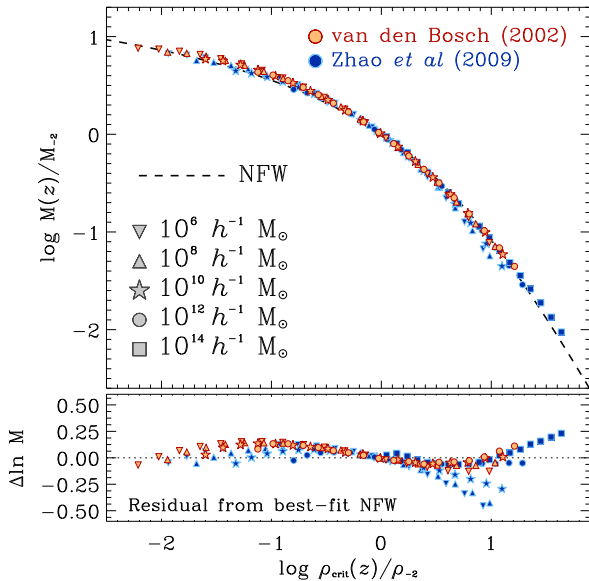


Figure 7. Mass accretion histories for dark matter halos predicted by the models of Zhao et al. (2009) (blue symbols) and van den Bosch (2002) (orange symbols), scaled to their best-fit NFW parameters: M_{-2} and $\rho_{\text{crit}}(z_{-2})$. Assembly histories are shown for halos spanning eight orders of magnitude in present-day mass, ranging from $10^6 h^{-1} M_{\odot}$ to $10^{14} h^{-1} M_{\odot}$. The dashed line shows the NFW profile, which is fixed in these units. Residuals from best-fit NFW profiles are shown in the bottom panel.

Monaco et al. 2013), or by calibrating empirical relations against the results of N-body simulations (Zhao et al. 2009).

For the purpose of estimating concentrations, we only need to specify the rate at which halos increase their mass with time, and therefore approximate methods that yield the ensemble average $\langle M(z)/M_0 \rangle$ for halos of a given mass M_0 would suffice. Because accretion histories are primarily a function of the dimensionless peak height, ν , MAHs that describe halos at $z = 0$ can easily be rescaled to describe the growth of halos identified at other redshifts. We are mainly interested in methods that reproduce, to good approximation, our finding that $M(\rho_{\text{crit}}(z))$ follows approximately the NFW profile. Although the literature is extensive, we focus here on two models that satisfy this criterion (van den Bosch 2002; Zhao et al. 2009), and refer the interested reader to those papers for a more comprehensive list of references.

The van den Bosch (2002) model (hereafter vdB, for short) is largely based on the extended Press-Schechter theory, whereas the Zhao et al. (2009) model has been constructed empirically from cosmological N-body simulations. As shown in Fig. 7, both predict NFW-like mass accretion history shapes. This figure shows predicted MAHs for halos spanning eight orders of magnitude in mass, after scaling them by their best fitting NFW parameters. The deviations from the NFW shape are quite small, typically less than 10-20% over two decades in $M(z)$. The predictions of the two models are essentially indistinguishable for halos above $\sim 10^8 M_{\odot}$, although the Zhao et al. (2009) model appears to deviate more strongly from NFW at smaller masses.

These deviations imply small differences in the predicted concentrations of low mass halos. Unfortunately, the

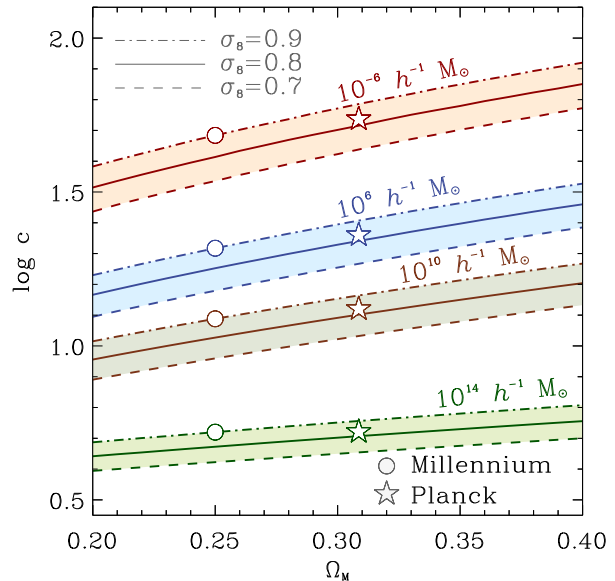


Figure 9. Concentration as a function of the matter density parameter, Ω_M , and the normalization of the matter power spectrum, σ_8 , for halos of four different masses: $10^{-6} h^{-1} M_{\odot}$ (red), $10^6 h^{-1} M_{\odot}$ (blue), $10^{10} h^{-1} M_{\odot}$ (brown) and $10^{14} h^{-1} M_{\odot}$ (green). Different line-styles correspond to different values of σ_8 , as indicated in the legend. We assume for all models a flat geometry, $\Omega_{\Lambda} = 1 - \Omega_M$. The remaining parameters assume values consistent with the latest Planck cosmology (see Table 2). Heavy symbols highlight the concentration values corresponding to the Millennium and Planck cosmologies, as indicated in the legend.

differences become appreciable only for masses smaller than those resolved by the Millennium Simulations, where the smallest halos for which we can reliably measure concentrations are of order $10^{10} M_{\odot}$. We therefore resort to higher resolution simulations of smaller volumes, such as those of the Aquarius Project (Springel et al. 2008). These simulations resolve volumes surrounding Milky Way-sized halos, and allow us to probe the mass-concentration relation of halos with masses as small as $10^5 M_{\odot}$ or so.

We show the result of this exercise in Fig. 8, where we plot the r_{max} vs V_{max} for all halos in our sample. (As discussed in Sec. 2.2, these parameters provide an alternative characterization of the mass and concentration of a halo.) We also plot all *isolated* halos in the high-resolution regions of the Aquarius simulations. These are defined to be the main halos of all FOF groups found at least three virial radii away from the center of the main Aquarius halo. This is done in order to ensure that all subhalos “associated” with the main halo are excluded from the analysis (Ludlow et al. 2009), since their concentrations and masses were likely modified by the tidal field of the main object.

The right-hand panel of Fig. 8 zooms-in on the low-mass halo regime resolved only by the Aquarius runs. We use the highest-resolution Aq-A-1 run in order to extend as much as possible the dynamic range of the comparison. All isolated high-resolution halos in the Aq-A volume are shown with grey points, together with their median values after grouping them by virial mass in bins of equal logarithmic width (solid squares). Grey lines show the loci of halos of constant

virial mass. A dot-dashed curve shows the predictions of the Zhao et al. (2009) model, a solid curve corresponds to the van den Bosch (2002) model, while a dashed line in black shows the simple power-law mass-concentration relation fitted by Neto et al. (2007) to dynamically relaxed MS-I halos.

Fig. 8 makes clear that all of these models reproduce extremely well the r_{\max} - V_{\max} relation over roughly ten decades in mass, although the van den Bosch (2002) model seems to outperform the others at very low masses. At $\sim 10^5 M_{\odot}$, the Neto et al. power-law predicts halos that are more concentrated⁷ than measured in the simulation, whereas the Zhao et al. model deviates in the opposite sense. Concentrations derived from accretion histories computed using the vdB model, on the other hand, seem to predict the median concentration as a function of mass accurately over the whole range in halo mass resolved by these simulations. We shall therefore, in what follows, adopt the vdB model in order to compute analytic estimates of the concentration that can be compared with the results of simulations. A description of the procedure may be found in the Appendix.

4.4 Predicted mass-concentration-redshift relation

Once a model for generating mass accretion histories has been adopted, it is straightforward to fit them with an NFW profile in order to predict concentrations for LCDM halos of arbitrary mass and at any redshift. The thick solid (red) lines in Fig. 1 shows the $c(M)$ relation at $z = 0, 1$, and 2 predicted by the vdB model, compared with the MS halo data. Together with Fig. 8, Fig. 1 demonstrates that the procedure works remarkably well at all z and at all masses, especially considering the simplicity of the model, which is based on fitting a single parameter to ensemble average accretion histories.

We can use the same model to explore the dependence of $c(M, z)$ on cosmological parameters. This is shown in Fig. 9, where we show how the median concentrations of 10^6 , 10^{10} and $10^{14} h^{-1} M_{\odot}$ halos at $z = 0$ depend on the matter-density parameter, Ω_M , and the fluctuation amplitude σ_8 , for a Universe with flat geometry (i.e., $\Omega_{\Lambda} = 1 - \Omega_M$; the other cosmological parameters are assumed to take the Planck cosmology values, see Table 2). This figure makes clear that the changes in concentration induced by varying the cosmological parameters is mass dependent, affecting more strongly low mass halos than massive systems.

The symbols in Fig. 9 show the predicted concentrations for halos in the Millennium Simulation cosmology and for the cosmological parameters favoured by latest analysis of the Planck satellite data (Planck Collaboration et al. 2013), respectively. At fixed mass, halo concentrations increase with both Ω_M and σ_8 and, as a result, concentrations derived from Millennium Simulation halos at $z = 0$ are actually very similar to those expected for the Planck cosmology. At 10^{10} and $10^{12} h^{-1} M_{\odot}$, for example, MS concentrations

should be corrected upward by only $\sim 7\%$ and 5% , respectively. For massive halos, with $M_0 \sim 10^{14} h^{-1} M_{\odot}$, both cosmological models predict $c \sim 5.3$.

The dependence of concentration on cosmology shown in Fig. 9 agrees well with earlier simulation work where different cosmological parameters were assumed. We show this explicitly in Fig. 10, where we compare the predictions of our model with the fitting formulae proposed by Duffy et al. (2008), Macciò et al. (2008) and Prada et al. (2012) for the WMAP5, WMAP3 and WMAP7 cosmologies, respectively. The dashed, dot-dashed and dashed lines show their fits, with thicker line type indicating the halo mass range actually resolved by each simulation. Our model is shown by the solid lines in Fig. 10 and is in good agreement with this earlier work.

Fig. 10 also makes clear that, at low masses, our predicted $c(M)$ relation deviates systematically from a power law, in a way that results in lower concentrations than expected from simply extrapolating the power-law fits obtained at higher masses. With hindsight, this is not surprising. The variance of the CDM power spectrum varies slowly at very low masses, implying a weak mass dependence of their formation histories and, therefore, similar concentration. At the other end of the mass scale, a similar reasoning explains why concentrations approach a constant value at very large halo masses (see Sec. 4.2).

The weak mass dependence of concentration at low masses might lead to important changes in the self-annihilation flux expected from low-mass halos, and to modifications in the importance of the “boost factor” from substructure, which is expected to dominate the annihilation luminosity (e.g. Kuhlen et al. 2008; Springel et al. 2008). We can estimate the magnitude of the effect by integrating the annihilation luminosity of a smooth NFW halo over the subhalo mass function $n(m_{\text{sub}})$ from the free-streaming limit of the CDM particle ($\sim 10^{-6} h^{-1} M_{\odot}$) up to the typical mass of the largest subhalo ($\sim 0.1 M_0$). For $n(m_{\text{sub}}) \propto m_{\text{sub}}^{-1.9}$ (Springel et al. 2008) and $M_0 \sim 10^{12} M_{\odot}$, we find that a simple extrapolation of the power-law $c(M)$ proposed by Neto et al. results in a boost factor that exceeds by a factor of ~ 20 that predicted by our model (see also Kuhlen et al. 2012). The actual magnitude of the correction to the boost factor is not straightforward to compute, however, since subhalo concentrations are known to be affected by the tidal field of the main halo and the boost depends in a complex manner on the subhalo-within-subhalo hierarchy. We defer a detailed study of this issue to a future paper.

5 SUMMARY AND CONCLUSIONS

We have used the Millennium Simulations, together with simulations of the Aquarius Project, to investigate the dependence of halo concentration on mass and redshift. This is a topic that has been studied repeatedly through numerical simulations, but whose understanding has so far eluded simple analytical modeling.

Our results confirm earlier claims that halo mass profiles are strongly linked to the mass accretion history (MAH) of their main progenitor and that the concentration of relaxed halos is solely a function of the dimensionless mass parameter, $\nu(M, z)$ (eq. (5)). MAHs and mass profiles have similar

⁷ We note that Springel et al. (2008) report good agreement between the Neto et al. power law and the Aquarius results. The (small) differences we remark upon here are due to the fact that we enforce a stricter “isolation” criterion and that we bin halos *by mass* rather than by V_{\max} before computing their median r_{\max} .

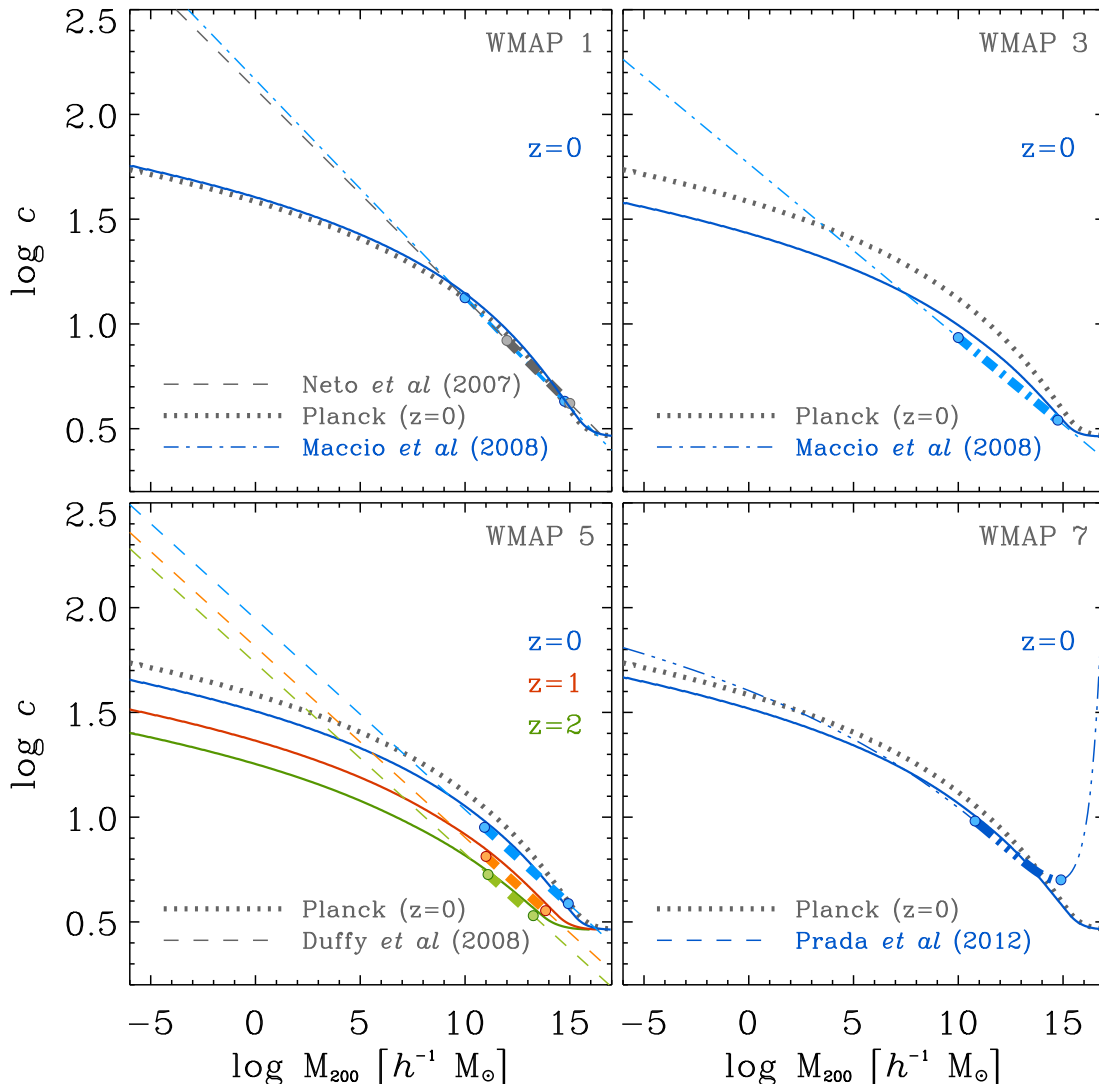


Figure 10. The concentration-mass relation from earlier simulation work that assumed different LCDM cosmological parameters. The top-left panel shows the results of two simulations at $z = 0$; one assuming the WMAP1 cosmological parameters, from Macciò et al. (2008), and the MS cosmology, from Neto et al. (2007). The top-right panel shows the $c(M)$ relation for the WMAP3 cosmology from Macciò et al. (2008). The bottom-left panel shows results for the WMAP5 cosmology from Duffy et al. (2008), and the bottom-right panel corresponds to the WMAP7 results from Prada et al. (2012). (We note that the Prada et al. (2012) model for $c(M, z)$ predicts a different redshift dependence than ours; we show here only results at $z = 0$.) The grey dotted line in each panel shows, for comparison, the predicted relation for the Planck cosmology. The values of the cosmological parameters used for each are listed in Table 2. In each panel, the dashed and dot-dashed lines indicate the fits proposed by these authors, with a thick line type indicating the halo mass range actually resolved in each simulation. When available, we have used the results quoted for relaxed halos by each author. Solid lines indicate the predictions of our model. Note that they describe very well the results of earlier work over their resolved halo mass range. Our model, however, predicts systematic deviations at the low-mass end compared with simple extrapolations of power-laws fits calibrated at higher masses.

shapes, and, for given mass, each one can be described on average by a single “concentration” parameter. This implies that accretion histories may be used to compute halo concentrations and vice versa. In practice, NFW profiles may be fit to MAHs and their parameters used to predict the mass profile concentration using eq. (6). Our analysis shows that this procedure predicts accurately the mass-concentration relation at all redshifts when MAHs are computed directly from simulations.

We have also explored whether analytical MAH models can be used to predict accurate concentrations. Although there are a number of MAH models in the literature, some of them are not applicable to our procedure, since they either adopt forms that do not depend solely on ν , or else predict MAHs that do not resemble NFW profiles. We find that a model based on the framework proposed by van den Bosch (2002) predicts halo concentrations that agree with simulations over a remarkable range of *ten decades* in halo mass. It

also predicts a dependence on cosmological parameters that agrees with published simulations of different variants of the LCDM cosmogony.

When extrapolated to low halos masses the model predicts systematically lower concentrations than expected from the power-law fits proposed in earlier work. This agrees with recent simulations of microhalo formation, which find concentrations of order ~ 60 -80 for $\sim 10^{-7} h^{-1} M_\odot$ halos at $z = 0$ (Anderhalden & Diemand 2013). Although further work on the structure of microhalos is clearly needed, our results make clear that care should be taken when extrapolating the $c(M)$ relation to extremely low masses, such as when computing the expected flux from self-annihilation, or the “boost factor” from substructure.

The model we propose here resolves the long-standing difficulties that have plagued earlier attempts to account analytically for the evolution of the mass-concentration relation. It clarifies and extends earlier models that link the concentration with particular features of the mass accretion history, and allows the dependence of concentrations on cosmological parameters to be estimated in a simple way. We present a step-by-step description of how to estimate the mass-concentration-redshift relation of LCDM halos in an Appendix. This is a simple tool that should be of use when interpreting observations that place constraints on the characteristic density of the dark halos that surround galaxies and galaxy systems.

ACKNOWLEDGEMENTS

We wish to thank Gerard Lemson for useful discussions, as well as the Virgo Consortium for access to the MS data. ADL acknowledges financial support from the SFB (956) from the Deutsche Forschungsgemeinschaft. V.S. acknowledges support by the DFG through Transregio 33, “The Dark Universe”. This work used the COSMA Data Centric system at Durham University, operated by the Institute for Computational Cosmology on behalf of the STFC DiRAC HPC Facility (www.dirac.ac.uk). This equipment was funded by a BIS National E-infrastructure capital grant ST/K00042X/1, DiRAC Operations grant ST/K003267/1 and Durham University. DiRAC is part of the National E-Infrastructure. We acknowledge partial financial support from by the National Science Foundation under Grant No. PHYS-1066293 and the hospitality of the Aspen Center for Physics.

This paper has been typeset from a \LaTeX file prepared by the author.

APPENDIX A: A MODEL FOR COMPUTING THE CONCENTRATION-MASS-REDSHIFT RELATION

Our model is based on the model for accretion histories of van den Bosch (2002). We provide here a simple summary of the basic features needed to compute $c(M, z)$ for LCDM halos, and refer the reader to the original paper for details. In this model, the *average* MAH of a halo of mass M_0 at $z = 0$ is approximated as follows:

$$\log \frac{M(z)}{M_0/2} = \left(\frac{\log(1+z)}{\log(1+z_f)} \right)^\chi, \quad (\text{A1})$$

where $z_f(M_0)$ is a characteristic “half-mass” formation time, and χ is a parameter that depends on cosmology and mass,

$$\chi = 1.211 + 1.858 \log(1+z_f) + 0.308 \Omega_\Lambda^2 - 0.032 \log(M_0/[10^{11} h^{-1} M_\odot]). \quad (\text{A2})$$

The “formation redshift”, z_f , is given by

$$\delta_{\text{crit}}(z_f) = \delta_{\text{crit}}(0) + 0.477 \sqrt{2[\sigma^2(f M_0) - \sigma^2(M_0)]}, \quad (\text{A3})$$

where $\delta_{\text{crit}}(z) = \delta_{\text{crit}}^0/D(z)$ (Lacey & Cole 1993) and $f = 0.068$ is a fitting parameter obtained empirically from fits to the MS accretion histories. $D(z)$ is the linear growth factor; and δ_{crit}^0 is the critical density threshold for spherical collapse at $z = 0$. The latter depends (very weakly) on cosmology and can be accurately approximated by $\delta_{\text{crit}}^0 = 0.15 (12\pi)^{2/3} \Omega_M^\kappa$, with

$$\kappa = \begin{cases} 0 & \text{if } \Omega_M = 1 \text{ and } \Omega_\Lambda = 0, \\ 0.0185 & \text{if } \Omega_M < 1 \text{ and } \Omega_\Lambda = 0, \\ 0.0055 & \text{if } \Omega_M + \Omega_\Lambda = 1. \end{cases} \quad (\text{A4})$$

This procedure fully specifies the assembly histories of halos identified at $z = 0$. We express them in terms of the dimensionless mass parameter, $\nu = \delta_{\text{crit}}/\sigma(M)$, and assume that this is the only relevant dependency in order to compute mass accretion histories for halos identified at any other redshift.

These mass accretion histories are then expressed as $M(\rho_{\text{crit}}(z))$ and fitted to the NFW mass-density profile given by eq. (4). The MAH concentration thus obtained is then converted into a predicted mass profile concentration using eq. (6).

REFERENCES

- Anderhalden D., Diemand J., 2013, JCAP, 4, 9
 Angulo R. E., Springel V., White S. D. M., Jenkins A., Baugh C. M., Frenk C. S., 2012, MNRAS, 426, 2046
 Angulo R. E., White S. D. M., 2010, MNRAS, 405, 143
 Bond J. R., Cole S., Efstathiou G., Kaiser N., 1991, ApJ, 379, 440
 Bower R. G., 1991, MNRAS, 248, 332
 Boylan-Kolchin M., Springel V., White S. D. M., Jenkins A., Lemson G., 2009, MNRAS, 398, 1150
 Bullock J. S., Kolatt T. S., Sigad Y., Somerville R. S., Kravtsov A. V., Klypin A. A., Primack J. R., Dekel A., 2001, MNRAS, 321, 559
 Dolag K., Bartelmann M., Perrotta F., Baccigalupi C., Moscardini L., Meneghetti M., Tormen G., 2004, A&A, 416, 853
 Duffy A. R., Schaye J., Kay S. T., Dalla Vecchia C., 2008, MNRAS, 390, L64
 Eisenstein D. J., Loeb A., 1996, ApJ, 459, 432
 Eke V. R., Navarro J. F., Steinmetz M., 2001, ApJ, 554, 114
 Gao L., Navarro J. F., Cole S., Frenk C. S., White S. D. M., Springel V., Jenkins A., Neto A. F., 2008, MNRAS, 387, 536
 Giocoli C., Tormen G., Sheth R. K., 2012, MNRAS, 422, 185

- Kauffmann G., White S. D. M., 1993, MNRAS, 261, 921
Kuhlen M., Diemand J., Madau P., 2008, ApJ, 686, 262
Kuhlen M., Vogelsberger M., Angulo R., 2012, Physics of the Dark Universe, 1, 50
Lacey C., Cole S., 1993, MNRAS, 262, 627
Lu Y., Mo H. J., Katz N., Weinberg M. D., 2006, MNRAS, 368, 1931
Ludlow A. D., Navarro J. F., Boylan-Kolchin M., Bett P. E., Angulo R. E., Li M., White S. D. M., Frenk C., Springel V., 2013, MNRAS, 432, 1103
Ludlow A. D., Navarro J. F., Li M., Angulo R. E., Boylan-Kolchin M., Bett P. E., 2012, MNRAS, 427, 1322
Ludlow A. D., Navarro J. F., Springel V., Jenkins A., Frenk C. S., Helmi A., 2009, ApJ, 692, 931
Ludlow A. D., Navarro J. F., Springel V., Vogelsberger M., Wang J., White S. D. M., Jenkins A., Frenk C. S., 2010, MNRAS, p. 718
Macciò A. V., Dutton A. A., van den Bosch F. C., 2008, MNRAS, 391, 1940
Monaco P., Sefusatti E., Borgani S., Croce M., Fosalba P., Sheth R. K., Theuns T., 2013, MNRAS, 433, 2389
Navarro J. F., Frenk C. S., White S. D. M., 1996, ApJ, 462, 563
Navarro J. F., Frenk C. S., White S. D. M., 1997, ApJ, 490, 493
Neto A. F., Gao L., Bett P., Cole S., Navarro J. F., Frenk C. S., White S. D. M., Springel V., Jenkins A., 2007, MNRAS, 381, 1450
Nusser A., Sheth R. K., 1999, MNRAS, 303, 685
Parkinson H., Cole S., Helly J., 2008, MNRAS, 383, 557
Planck Collaboration Ade P. A. R., Aghanim N., Armitage-Caplan C., Arnaud M., Ashdown M., Atrio-Barandela F., Aumont J., Baccigalupi C., Banday A. J., et al. 2013, ArXiv e-prints: 1303.5076
Power C., Navarro J. F., Jenkins A., Frenk C. S., White S. D. M., Springel V., Stadel J., Quinn T., 2003, MNRAS, 338, 14
Prada F., Klypin A. A., Cuesta A. J., Betancort-Rijo J. E., Primack J., 2012, MNRAS, 423, 3018
Press W. H., Schechter P., 1974, ApJ, 187, 425
Sheth R. K., Lemson G., 1999, MNRAS, 305, 946
Somerville R. S., Kolatt T. S., 1999, MNRAS, 305, 1
Springel V., Wang J., Vogelsberger M., Ludlow A., Jenkins A., Helmi A., Navarro J. F., Frenk C. S., White S. D. M., 2008, MNRAS, 391, 1685
Springel V., White S. D. M., Frenk C. S., Navarro J. F., Jenkins A., Vogelsberger M., Wang J., Ludlow A., Helmi A., 2008, Nature, 456, 73
Springel V., White S. D. M., Jenkins A., Frenk C. S., Yoshida N., Gao L., Navarro J., Thacker R., Croton D., Helly J., Peacock J. A., Cole S., Thomas P., Couchman H., Evrard A., Colberg J., Pearce F., 2005, Nature, 435, 629
Springel V., White S. D. M., Tormen G., Kauffmann G., 2001, MNRAS, 328, 726
Taffoni G., Monaco P., Theuns T., 2002, MNRAS, 333, 623
van den Bosch F. C., 2002, MNRAS, 331, 98
Wang J., Navarro J. F., Frenk C. S., White S. D. M., Springel V., Jenkins A., Helmi A., Ludlow A., Vogelsberger M., 2011, MNRAS, 413, 1373
Wechsler R. H., Bullock J. S., Primack J. R., Kravtsov A. V., Dekel A., 2002, ApJ, 568, 52
Zhao D. H., Jing Y. P., Mo H. J., Börner G., 2003, ApJL, 597, L9
Zhao D. H., Jing Y. P., Mo H. J., Börner G., 2009, ApJ, 707, 354